

RESEARCH ARTICLE | JUNE 15 2023

A model heterostructure with engineered Berry curvature ^{EP}

Nathaniel J. Schreiber ^{ID}; Ludi Miao ^{ID}; Berit H. Goodge ^{ID}; Lena F. Kourkoutis ^{ID}; Kyle M. Shen ^{ID}; Darrell G. Schlom [✉] ^{ID}



APL Mater 11, 061117 (2023)

<https://doi.org/10.1063/5.0151126>



CrossMark

Export Citation



yttrium iron garnet, zeolites, nano ribbons, sapphire windows, spintronics, silver nanoparticles, MOCVD, rare earth metals, osmium, refractory metals, anodic aluminum oxide, niobate, InAs wafers, MOFs, AuNPs, ZnS, CdTe, perovskite crystals, transparent ceramics

cerium oxide polishing powder, surface functionalized nanoparticles, cerium oxide, beta-barium borate, quantum dots, scintillation Ce:YAG, laser crystals, niobate, InAs wafers, MOFs, AuNPs, ZnS, CdTe, transparent ceramics

glassy carbon, beamsplitters, fused quartz, additive manufacturing, zeolites, III-IV semiconductors, gallium lump, copper nanoparticles, organometallics, nano ribbons, barium fluoride, europium phosphors, photonics, infrared dyes, epitaxial crystal growth, ultra high purity materials, transparent ceramics, CIGS, cermet, nanodispersions, MBE grade materials, thin film, OLED lighting, solar energy, sputtering targets, fiber optics, h-BN, deposition slugs, CVD precursors, photovoltaics, metamaterials, borosilicate glass, YBCO superconductors, InGaAs, indium tin oxide, MgF2, rutile, diamond micropowder, optical glass

THE ADVANCED MATERIALS MANUFACTURER®

Now Invent.™

www.americanelements.com

© 2001-2022, American Elements LLC, a U.S. Registered Trademark



A model heterostructure with engineered Berry curvature

Cite as: APL Mater. 11, 061117 (2023); doi: 10.1063/5.0151126

Submitted: 18 March 2023 • Accepted: 9 May 2023 •

Published Online: 15 June 2023



View Online



Export Citation



CrossMark

Nathaniel J. Schreiber,¹  Ludi Miao,²  Berit H. Goodge,³  Lena F. Kourkoutis,^{3,4}  Kyle M. Shen,^{2,4} 
and Darrell G. Schlom^{1,4,5,a)} 

AFFILIATIONS

¹Department of Materials Science and Engineering, Cornell University, Ithaca, New York 14853, USA

²Department of Physics, Laboratory of Atomic and Solid State Physics, Cornell University, Ithaca, New York 14853, USA

³School of Applied and Engineering Physics, Cornell University, Ithaca, New York 14853, USA

⁴Kavli Institute at Cornell for Nanoscale Science, Ithaca, New York 14853, USA

⁵Leibniz-Institut für Kristallzüchtung, Max-Born-Str. 2, 12489 Berlin, Germany

^{a)}Author to whom correspondence should be addressed: schlom@cornell.edu

ABSTRACT

Molecular-beam epitaxy enables ultrathin functional materials to be combined in heterostructures to create emergent phenomena at the interface. Magnetic skyrmions are an example of an exciting phase found in such heterostructures. SrRuO₃ and SrRuO₃-based heterostructures have been at the center of the debate on whether a hump-like feature appearing in Hall resistivities is sufficient evidence to prove the presence of skyrmions in a material. To address the ambiguity, we synthesize a model heterostructure with engineered Berry curvature that combines, in parallel, a positive anomalous Hall effect (AHE) channel (a Sr_{0.6}Ca_{0.4}RuO₃ layer) with a negative AHE channel (a SrRuO₃ layer). We demonstrate that the two opposite AHE channels can be combined to artificially reproduce a “hump-like” feature, which closely resembles the hump-like feature typically attributed to the topological Hall effect and the presence of chiral spin textures, such as skyrmions. We compare our heterostructure with a parallel resistor model, where the inputs are the AHE data from individual Sr_{0.6}Ca_{0.4}RuO₃ and SrRuO₃ films. To check for the presence of skyrmions, we measure the current dependence, angle dependence, and minor loop dependence of R_{hump} in the heterostructure. Despite the clear hump, no evidence of skyrmions is found.

© 2023 Author(s). All article content, except where otherwise noted, is licensed under a Creative Commons Attribution (CC BY) license (<http://creativecommons.org/licenses/by/4.0/>). <https://doi.org/10.1063/5.0151126>

I. INTRODUCTION

The ordinary Hall effect (OHE) is generated when an external magnetic field is applied to a conductive material.¹ Other than the OHE, there are many other Hall effects, including the anomalous Hall effect (AHE)² and the topological Hall effect (THE).³ While the OHE requires an external magnetic field, the AHE and THE arise spontaneously. The anomalous Hall effect has extensively been studied, and it is known to emerge spontaneously in materials with broken time-reversal symmetry, for example, in ferromagnets.^{2,4} Typically, the AHE is observed as a hysteretic “box-like” signal in the Hall measurement. The topological Hall effect emerges when electrons are able to acquire a Berry phase while moving through a material with a chiral spin texture, for example,

magnetic skyrmions.³ It is possible to measure magnetic skyrmions using techniques such as Lorentz transmission electron microscopy,⁵ magnetic force microscopy,⁶ and small-angle neutron scattering.⁷ Nonetheless, the THE is typically inferred by the presence of a spontaneous “hump-like” feature that appears in the anomalous Hall effect measurement.

Recently, SrRuO₃ and SrRuO₃-based heterostructures have become the focus of a debate surrounding the hump-like feature, THE, and skyrmions.⁸ Matsuno *et al.*⁹ published the discovery of an interface-driven THE in a SrRuO₃-SrIrO₃ bilayer structure and theorized that the hump-like feature in their magnetotransport measurement was due to the presence of Néel-type skyrmions. Since this publication, a further investigation using magnetic force microscopy has shown small bubble domains to be present in

SrIrO₃/SrRuO₃ bilayers made up of a 2 pseudocubic unit cell (u.c.) thick SrIrO₃ layer grown on top of a 10 u.c. thick SrRuO₃ layer,¹⁰ where the growth direction of the bilayer is the [001] pseudocubic direction of the perovskites. Unfortunately, the evidence remains inconclusive that these bubbles are skyrmions.⁸ Many other studies have reported similar hump-like features in SrRuO₃ thin films and heterostructures.^{11–13} Meanwhile, others have argued that the hump can also appear as an artifact in materials or material systems that are inhomogeneous,^{14–16} are strain-relaxed,¹⁷ contain ruthenium vacancies,¹⁸ or generally have two (or more) mixed, anomalous Hall effect channels of different magnitudes and opposite sign.^{19–22} For example, if there is a large positive AHE channel and a small negative AHE channel, one can measure a net positive AHE signal with a hump-like feature on top.⁸ This hump-like feature is indistinguishable from the THE hump, which is currently used as a signature measurement for skyrmion detection. Therefore, while it seems to be true that materials with skyrmions typically have the hump-like feature, the converse is not necessarily true: materials that exhibit the hump-like feature do not necessarily host skyrmions. Thus, more direct measurements are necessary in order to confirm the presence of skyrmions in a material.

In this work, we artificially reproduce the hump-like feature in Hall resistivity measurements by synthesizing a model heterostructure with engineered Berry curvature. The heterostructure is a bilayer, consisting of one layer with positive AHE sign and one layer with negative AHE sign, as shown in Fig. 1, of distinct magnitudes. In other words, the heterostructure in total has two major AHE channels, one in each layer. We are able to tailor the sign of the AHE in each layer of the heterostructure by controlling the amount of calcium substituted for strontium in the solid solution Sr_{1-x}Ca_xRuO₃, as shown in Miao *et al.*²³ Thus, we can create a Berry curvature heterostructure by interfacing SrRuO₃ and Sr_{0.6}Ca_{0.4}RuO₃, two isostructural materials, but with anomalous Hall effects of opposite sign. We demonstrate that each layer individually does not show the hump-like hysteresis associated with the AHE. Nonetheless, when the layers are combined in the heterostructure, the hump-like

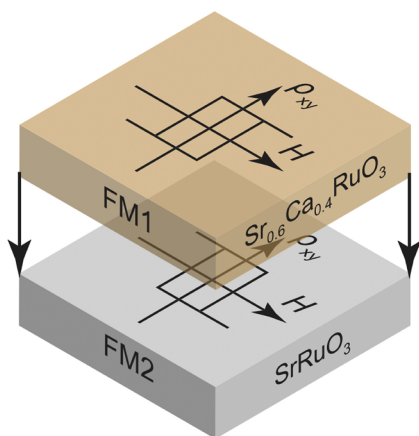


FIG. 1. An illustration showing the concept of a model heterostructure with engineered Berry curvature, where a positive anomalous Hall effect (AHE) material is interfaced with a negative AHE material.

feature emerges. Using current dependence, angle dependence, and minor loop dependence measurements, we confirm that the hump-like feature is not due to the presence of skyrmions. In addition, we utilize a parallel resistor model to demonstrate that the effect can be attributed to the mixing of two AHE signals and is not an emergent property of the interface. This experiment on a model interface represents a clear demonstration of how the hump-like feature can be artificially generated by multi-channel anomalous Hall effects, further supporting the premise that a hump-like feature is insufficient evidence to demonstrate the presence of skyrmions.

II. METHODS

A. Sample growth

Thin films of SrRuO₃ and Sr_{0.6}Ca_{0.4}RuO₃ were grown on (100) (LaAlO₃)_{0.29}-(SrAl_{1/2}Ta_{1/2}O₃)_{0.71} (LSAT) substrates by oxide molecular-beam epitaxy (MBE) in a Veeco Gen10 MBE system. The two individual films were grown to 14 u.c. thick. The absorption-controlled growth was optimized utilizing the previously published thermodynamics of MBE (TOMBE) diagram.²⁴ Films were grown at a substrate temperature of 650 °C and at a chamber pressure of 10⁻⁶ Torr in a distilled ozone environment (~80% O₃ + 20% O₂). The substrate temperature was measured using an optical pyrometer operating at a wavelength of 1550 nm. The strontium (99.99%) and calcium (99.99%) source materials were evaporated from low-temperature effusion cells, and an electron beam evaporator was used to deposit the ruthenium source material (99.99%). A bilayer heterostructure was also grown using the same conditions as were used for the two individual thin films on (100) LSAT. It is known that as the calcium concentration, or “x,” is increased in the solid solution Sr_{1-x}Ca_xRuO₃, the magnetic coercivity of the materials decreases.²³ Therefore, the coercivity of SrRuO₃ (x = 0) is larger than that of Sr_{0.6}Ca_{0.4}RuO₃ (x = 0.4). Nonetheless, to ensure that the as-grown heterostructure had sufficiently different coercivities in each of the layers, the x = 0.4 layer was grown thinner and the x = 0 layer was grown thicker than 14 u.c. to further enhance the disparity in coercivity. The nominal structure of the bilayer from the surface to the substrate is 10 u.c. of x = 0.4 on top of 18 u.c. of x = 0 on top of the (100) LSAT substrate, or when written in shorthand: Sr_{0.6}Ca_{0.4}RuO₃[10 u.c.]/SrRuO₃[18 u.c.]/LSAT(100). For the remainder of the paper, this bilayer sample will be referred to as the “heterostructure” for simplicity.

B. Sample characterization

For the resistivity and Hall measurements, the SrRuO₃ [14 u.c.]/LSAT(100) film, the Sr_{0.6}Ca_{0.4}RuO₃[14 u.c.]/LSAT(100) film, and the heterostructure were fabricated into Hall bars all with 20 × 50 μm² channels defined by photolithography. The channels were formed by argon ion milling, and platinum/titanium pads were subsequently sputtered onto the thin films to form ohmic contacts.

Transport measurements were performed in a quantum design physical property measurement system (PPMS). The AHE measurements of the 14 u.c. thick SrRuO₃ and 14 u.c. thick Sr_{0.6}Ca_{0.4}RuO₃ films were done in the aforementioned PPMS by measuring the transverse resistivity (ρ_{xy}) on the patterned Hall bars while applying a magnetic field perpendicular to the sample surface. For each AHE measurement at a given temperature, the applied magnetic field was

swept between -4 and 4 T. The measurement of the heterostructure was performed using these same parameters.

Cross-sectional scanning transmission electron microscopy (STEM) specimens were prepared by standard focused ion beam (FIB) lift-out with a Thermo Fisher Scientific Helios G4 UX FIB. High-angle annular dark-field scanning transmission electron microscopy (HAADF-STEM) images were acquired on an aberration-corrected FEI Titan Themis 300 operating at 300 kV with a 30 mrad probe convergence semi-angle and inner (outer) collection angle of 68 (340) mrad. Electron energy loss spectroscopy (EELS) mapping was performed under the same operating conditions on the same instrument equipped with a 965 GIF Quantum ER energy filter and a Gatan K2 Summit direct electron detector operated in the electron counting mode. The concentration maps for strontium, ruthenium, and calcium were obtained through a non-negative least squares fit to the weighted sum of reference spectra for each element over a range of 270–361 eV. The reference components used and the resulting score maps are shown in Fig. S1 of the supplementary material. The reference component for strontium was obtained from the average signal summed over the substrate region of the original EELS map. References for ruthenium and calcium are from the Gatan EELS Atlas and acquired from measurements of RuO_2 and CaCoO_3 , respectively. The inelastic backgrounds of all spectra are modeled with exponential fits and subtracted prior to this analysis.

III. RESULTS AND DISCUSSION

A. Basic characterization of the thin films and heterostructure

The 14 u.c. thick SrRuO_3 and $\text{Sr}_{0.6}\text{Ca}_{0.4}\text{RuO}_3$ thin films grown on LSAT(100) were confirmed to be phase pure by x-ray diffraction and were found to be metallic for the entire temperature range of 2.5–300 K, as shown in Figs. S2(a) and S2(c) of the supplementary material.²³ The two individual films were then measured in the Hall geometry described above. We find that the 14 u.c. thick SrRuO_3 film shows a negative AHE in both the low-temperature ($T = 40$ K) and the high-temperature ($T = 80$ K) measurements, as shown in Figs. 2(a) and 2(b), respectively. As for the 14 u.c. thick $\text{Sr}_{0.6}\text{Ca}_{0.4}\text{RuO}_3$ film, the Hall measurements at 40 and 80 K are shown in Figs. 2(c) and 2(d), respectively. This $\text{Sr}_{0.6}\text{Ca}_{0.4}\text{RuO}_3$ film exhibits a positive AHE signal at 40 K but no observable AHE signal was exhibited at 80 K (no observable hysteresis). Therefore, at 40 K, both films have an AHE signal, but of opposite sign and magnitude, and at 80 K, only the SrRuO_3 has an observable negative AHE signal. When comparing the AHE signals at 40 K, it is clear that the two films exhibit differences in the magnitude of the AHE signal and that the SrRuO_3 film has a much larger coercive field than the $\text{Sr}_{0.6}\text{Ca}_{0.4}\text{RuO}_3$ film. The combination of these two AHE signals provides an opportunity to create a Berry curvature heterostructure to investigate the hump-like feature in multi-channel AHE samples.

Specifically, we combined the SrRuO_3 film (negative AHE) with the $\text{Sr}_{0.6}\text{Ca}_{0.4}\text{RuO}_3$ film (positive AHE) in a bilayer heterostructure, which we grew on a (100) LSAT substrate. The concept of the heterostructure, which is to create an interface between two materials with Berry curvatures of opposite sign, is shown in Fig. 1. The heterostructure was characterized by STEM-EELS to confirm the quality of the interface, the chemical composition, and the

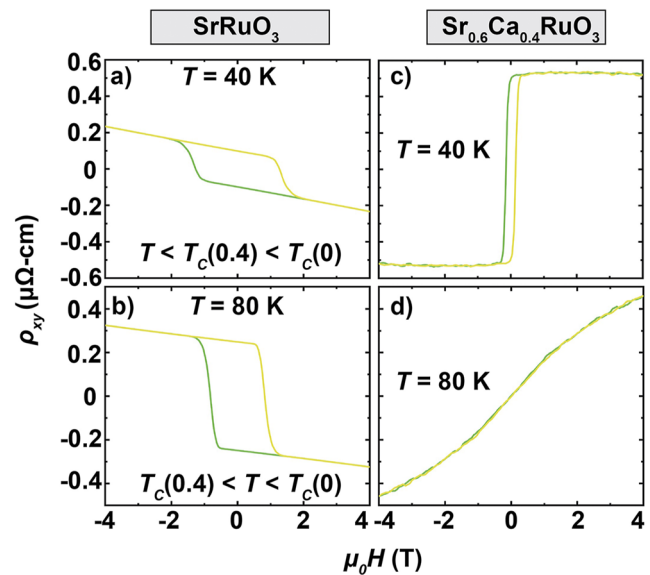


FIG. 2. AHE measurements at $T = 40$ K and $T = 80$ K of the individual thin films: (a) and (b) SrRuO_3 [14 u.c.]/LSAT(100) and (c) and (d) $\text{Sr}_{0.6}\text{Ca}_{0.4}\text{RuO}_3$ [14 u.c.]/LSAT(100), respectively.

microstructure of each of the layers. Figure 3(a) shows a HAADF-STEM image, demonstrating a sharp substrate–film interface and coherent crystallinity across both layers. The $\text{Sr}_{0.6}\text{Ca}_{0.4}\text{RuO}_3$ layer shows a slightly darker contrast than the SrRuO_3 layer due to the lower average Z of the A -sites in the doped structure ($\text{Ca} = 20$, $\text{Sr} = 38$). The layers are more clearly distinguished by EELS mapping, also shown in Fig. 3(a). The concentrations of spectral components assigned to calcium, strontium, and ruthenium are shown in an atomic-resolution two-dimensional score map and integrated parallel to the interface to produce vertical concentration profiles along the growth direction of the heterostructure. There appears to be a transition region of 1–2 u.c. at the interface between the $x = 0$ and $x = 0.4$ materials where the calcium is at a lower nominal concentration than the $\text{Sr}_{0.6}\text{Ca}_{0.4}\text{RuO}_3$ layer above it. Nevertheless, it is clear based on these measurements that there is a region of only strontium and ruthenium, which corresponds to the SrRuO_3 layer, and that in the $\text{Sr}_{0.6}\text{Ca}_{0.4}\text{RuO}_3$ layer, strontium, ruthenium, and calcium are all present.

We measured the resistance of the heterostructure as a function of temperature upon cooling, which is shown in Fig. 3(b). The heterostructure is metallic over the entirety of the temperature range shown. The first derivative with respect to temperature of the resistivity data is shown in the bottom half of Fig. 3(b), with the ferromagnetic Curie temperature (T_c) of each layer ($x = 0$ and $x = 0.4$) marked with an arrow, as determined in Miao *et al.*²³ and shown in Fig. S2 of the supplementary material. In SrRuO_3 , kinks in the resistivity vs temperature measurement are typically associated with T_c . In a bare SrRuO_3 film, there will be one kink in the data since there is only one ferromagnetic transition. Importantly, in Fig. 3(b), we find that there are two kinks, although the kink from the $x = 0.4$ layer is much less prominent due to the presence of two ferromagnetic layers with two different T_c values. SrRuO_3 has the higher T_c (T_{c0}) of

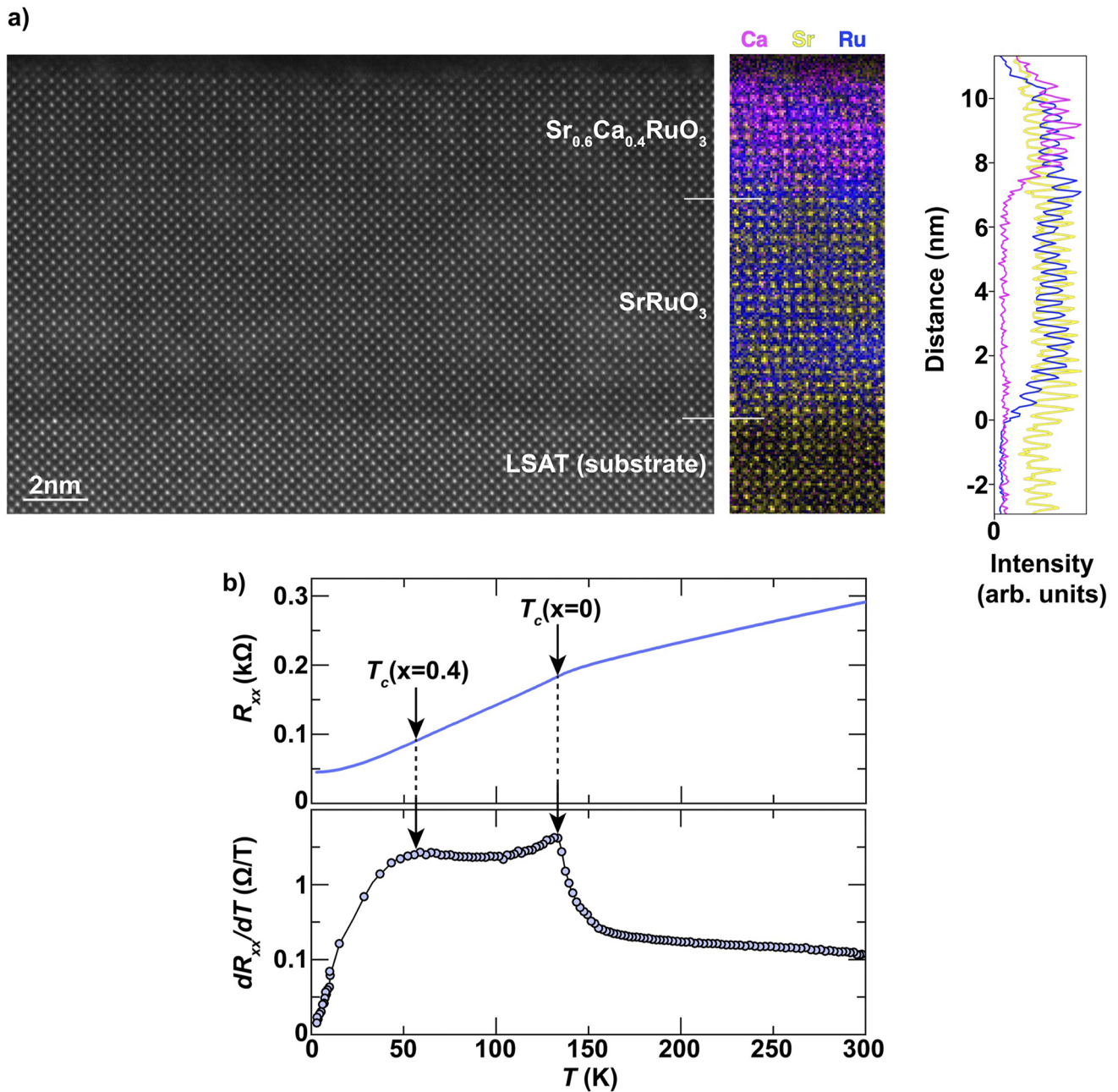


FIG. 3. (a) A scanning transmission electron microscopy (STEM) image of the same heterostructure that is the focus of this letter confirms the structural quality and similarity of both layers. Atomic-resolution mapping by electron energy loss spectroscopy (EELS) confirms the chemical separation, further evidenced by the horizontally integrated line profiles of strontium, calcium, and ruthenium component concentrations at right. (b) Resistance of the same heterostructure measured from 300 to 2.5 K. The heterostructure is metallic over the entire range. The bottom panel shows the first derivative of the measurement in the top panel with respect to temperature. The first derivative reveals the Curie temperature (T_c) of the heterostructure. In this case, there are two because there are two layers with different T_c s. $T_c(x=0.4)$ is the T_c of $\text{Sr}_{0.6}\text{Ca}_{0.4}\text{RuO}_3$ and $T_c(x=0)$ is the T_c of SrRuO_3 .

~ 139 K, and as calcium is substituted, the T_c is lowered such that the T_c of $\text{Sr}_{0.6}\text{Ca}_{0.4}\text{RuO}_3$ ($T_{c0.4}$) is ~ 55 K.²³ The presence of the two T_c values is another confirmation that the two layers are chemically different, and it allows for the ferromagnetic ordering of the two layers to be tuned separately by varying the temperature. For instance, at 200 K, neither layer is ferromagnetic, while at 80 K, the SrRuO_3 layer is ferromagnetic and the $\text{Sr}_{0.6}\text{Ca}_{0.4}\text{RuO}_3$ layer is still in the paramagnetic state. At 40 K, both layers are ferromagnetically ordered. Another method for switching the layers on and off preferentially is by utilizing the difference in the two coercive fields (H_c). As mentioned before, SrRuO_3 ($x = 0$) has a higher coercive field than $\text{Sr}_{0.6}\text{Ca}_{0.4}\text{RuO}_3$ ($x = 0.4$); therefore, we can magnetize both layers and preferentially demagnetize and switch the $x = 0.4$ layer without influencing the magnetization of the $x = 0$ layer.

B. Hall measurements

We fabricated Hall bars on the heterostructure using the steps outlined in Sec. II and then measured the Hall effect of the heterostructure [see Fig. 4(a)]. Note that the so-called hump-like feature starts to appear as the heterostructure is cooled through $T_{c0.4}$. The decrease in the hump signal as the sample is cooled below 40 K is difficult to explain. One observation is that the magnitude of the AHE signal, shown in Fig. 4(b), is decreasing with temperature starting at around 60 K when it is mostly negative. The hump is highest at 20–50 K and peaks at 40 K [see Fig. 4(c)], which is just under $T_{c0.4}$. Since the hump comes from the two AHE signals, most likely the decrease in the hump signal below 40 K can be derived from the decrease in the magnitude of the AHE signal.

C. Comparison of the model and the heterostructure

To further analyze the hump-like feature of the heterostructure sample, we can compare it to a parallel resistor model in which

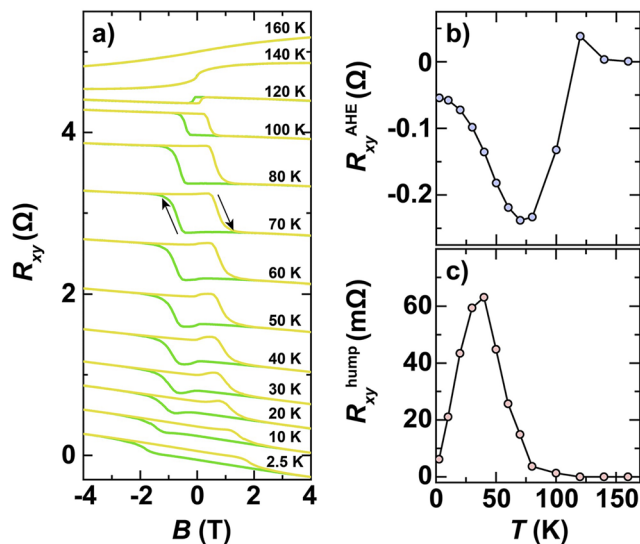


FIG. 4. (a) The anomalous Hall effect (AHE) of the heterostructure is measured at various temperatures. (b) The AHE signal from (a) is measured and plotted as a function of temperature. (c) The hump signal from (a) is measured and plotted as a function of temperature. The hump-like feature begins to appear upon cooling at around 70 K, and peaks at 40 K.

the inputs are the AHE data from the individual thin films: SrRuO_3 [14 u.c.]/LSAT(100) and $\text{Sr}_{0.6}\text{Ca}_{0.4}\text{RuO}_3$ [14 u.c.]/LSAT(100), shown in Figs. 2(a)–2(d), and mentioned previously. We took the AHE data from the two individual films and included them in a parallel resistor model to mimic the bilayer heterostructure. This simulation is shown in Figs. 5(a) and 5(b). Here, we are simulating how the AHE data would look if we assume there are no significant emergent properties at the interface, or in other words, it is a clear method of combining two AHE signals. We compare this simulation to our heterostructure data to understand how the hump-like feature emerges. Is it an interface effect, or can it be explained by simply combining two AHE signals? By comparing the model, Figs. 5(a) and 5(b), with the actual heterostructure, Figs. 5(c) and 5(d), at the two temperatures, hump ($T = 40$ K) vs no hump ($T = 80$ K), it is clear that the model and the actual heterostructure are qualitatively very similar. First, both show the hump at 40 K and not at 80 K. Therefore, in both the model and the heterostructure, the hump-like feature can be turned on and off with temperature. Second, the net sign of the AHE is negative for both the heterostructure and the model. From this, one can conclude that the same hump that is shown in the heterostructure can emerge by simply mixing two AHE signals of opposite sign. We think that the slight differences in the absolute amplitude and the shape of the hump between the model and the heterostructure could come from defects or slight calcium intermixing at the interface between the $x = 0$ and $x = 0.4$ layers. In addition, as mentioned in the supplementary material, the model is a simple parallel resistor model and is meant only to validate the concept of two parallel resistors of opposite AHE sign, yielding a hump-like feature in the Hall measurement.

D. Ruling out skyrmions

In order to rule out the possibility that the heterostructure contains skyrmions, we followed the method described by Kan *et al.*¹⁴ and measured the dependence of R_{hump} on the current density, the canting angle of the magnetic field, and minor field loops.¹⁷ The current-dependent Hall measurements are shown in Fig. 6(a) at three different currents. These measurements basically overlap. To show this more clearly, we plot R_{hump} at various current densities in Fig. 6(b). There is no current dependence on R_{hump} . If magnetic skyrmions were present in this heterostructure, one would expect R_{hump} to be strongly dependent on current and to decrease at higher current densities.²⁵ Next, we measured the dependence of the Hall resistivity at various field canting angles (θ), as shown in Fig. 6(c). Similar to the current dependence, when R_{hump} is plotted as a function of the canting angle [Fig. 6(d)], there seems to be little to no dependence up to angles as high as 50° . Ohuchi *et al.*²⁶ showed in EuO that the THE is strongly dependent on the tilting of the applied magnetic field, which we do not observe in our heterostructure measurements. Finally, the dependence of the Hall resistivity on the minor field loops is measured and shown in Figs. 6(e) and 6(f). Here, a closed-loop field sweep is applied, where each loop starts at the same maximum, B_{max} , of 4 T to saturate the AHE and potential THE fully. The applied magnetic field is then swept to impart the desired B_{min} . The B_{min} is increased (from a negative magnetic field toward a 0 magnetic field) in each subsequent loop. Minor field loops have been used similarly

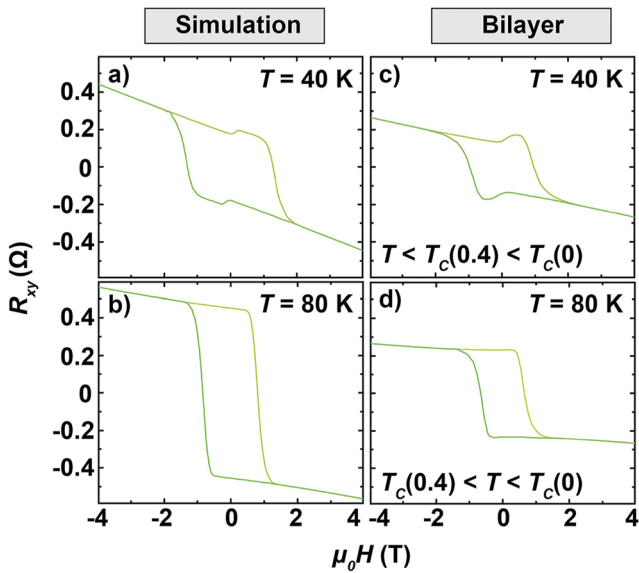


FIG. 5. AHE measurements at $T = 40$ K and $T = 80$ K for (a,b) the parallel resistor model and (c) and (d) the heterostructure sample, respectively. The data from the individual SrRuO_3 [14 u.c.]/LSAT(100) and $\text{Sr}_{0.6}\text{Ca}_{0.4}\text{RuO}_3$ [14 u.c.]/LSAT(100) thin films (shown in Fig. 2) are input into a parallel resistor model simulation, the result of which is shown in (a) and (b), and compared to the actual bilayer heterostructure at the same temperatures in (c) and (d). Indeed, as compared to the experimental bilayer data, the simulation shows a similar hump, at a similar applied field, and of similar magnitude. In addition, the net sign of the AHE is negative for both the model and the heterostructure.

in previous publications.^{14,17} It is apparent in Fig. 6(e) that the hump-like feature depends on the path taken in the various loops, and R_{hump} falls off dramatically when B_{min} is not fully saturating the potential THE in the negative direction, i.e., when $|B_{\text{min}}| < |B_{\text{hump, saturation}}|$. Therefore, the hump-like feature in our heterostructure is hysteretic, and as Kan *et al.*¹⁴ note, hysteresis is not congruent with the skyrmion picture.

IV. CONCLUSION

In summary, we have artificially created a hump-like feature in a model heterostructure with engineered Berry curvature and demonstrated that this hump-like feature is the direct result of mixing two AHE channels of opposite sign and not caused by the presence of skyrmions. Our bilayer model is a simplified case, in which we assume that the AHE properties change sharply across the interface. In reality, however, all samples are inhomogeneous to some degree, and therefore, the heterostructure should have a more continuous change in AHE properties near the interface than our simulation does. Furthermore, in the simulation of this heterostructure, the two layers are in parallel. In a real material, however, there are “puddles” of differing AHE signals that are nested together, most likely yielding a mixture of series and parallel resistors. Nevertheless, we expect that our simple model can still be applied to better understand real materials where the hump-like feature is observed. Berry curvature heterostructures, like the one at the heart of this study, could enable the exploration of more exotic states at interfaces in the future.

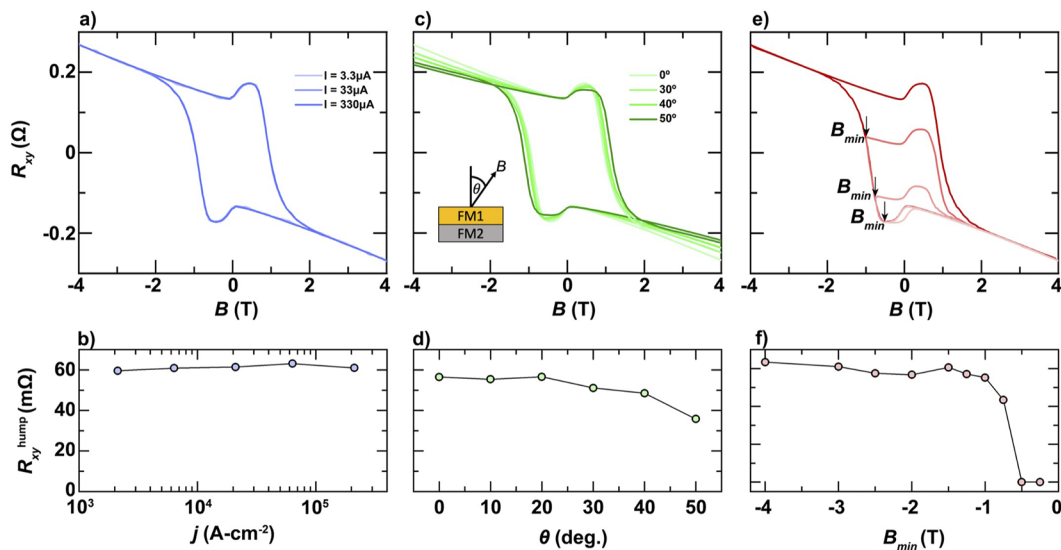


FIG. 6. (a) Transverse resistance, R_{xy} , measured at various currents in a magnetic field applied perpendicular to the sample surface. The three measurements almost perfectly overlap. (b) R_{hump} is plotted vs the current density, showing that there is no current dependence to R_{hump} . (c) R_{xy} measured at various field canting angles. (d) R_{hump} is plotted vs the canting angles (θ) up to 50° . Skyrmions should be sensitive to canting angle, and according to Ohuchi *et al.*,²⁵ the THE signal should drop off dramatically even at lower angles. (e) Minor loops of R_{xy} , measured with various B_{min} . (f) R_{hump} as a function of B_{min} . There is a clear drop in R_{hump} when B_{min} approaches the $-B_{\text{hump}}$ value. Hysteretic behavior like this is not consistent with the presence of skyrmions.¹⁴

SUPPLEMENTARY MATERIAL

Additional data and characterization relevant to this article and referenced in the main text—including Figs. S1 and S2—are provided in the supplementary material.

ACKNOWLEDGMENTS

This work was supported by the National Science Foundation Platform for the Accelerated Realization, Analysis, and Discovery of Interface Materials (PARADIM) under Cooperative Agreement No. DMR-2039380. This research was funded in part by the Gordon and Betty Moore Foundation's EPiQS Initiative through Grant Nos. GBMF3850 and GBMF9073 to Cornell University. Sample preparation was, in part, facilitated by the Cornell NanoScale Facility, a member of the National Nanotechnology Coordinated Infrastructure (NNCI), which is supported by the National Science Foundation (Grant No. NNCI-2025233). This work made use of the Cornell Center for Materials Research (CCMR) Shared Facilities, which are supported through the NSF MRSEC Program (Grant No. DMR-1719875). The FEI Titan Themis 300 was acquired through Grant No. NSF-MRI-1429155, with additional support from Cornell University, the Weill Institute, and the Kavli Institute at Cornell. The Thermo Fisher Helios G4 UX FIB was acquired with support by NSF Grant No. DMR-1539918. The authors thank Sean Christopher Palmer for his assistance with substrate preparation.

AUTHOR DECLARATIONS

Conflict of Interest

The authors have no conflicts to disclose.

Author Contributions

N.J.S. and L.M. contributed equally to this work.

Nathaniel J. Schreiber: Conceptualization (equal); Formal analysis (equal); Investigation (equal); Methodology (equal); Writing – original draft (equal); Writing – review & editing (equal). **Ludi Miao:** Conceptualization (equal); Investigation (equal); Methodology (equal); Writing – original draft (supporting); Writing – review & editing (equal). **Berit H. Goodge:** Formal analysis (supporting); Investigation (supporting); Methodology (supporting); Writing – original draft (supporting); Writing – review & editing (equal). **Lena F. Kourkoutis:** Funding acquisition (equal); Supervision (equal); Writing – review & editing (equal). **Kyle M. Shen:** Funding acquisition (equal); Supervision (equal); Writing – review & editing (equal). **Darrell G. Schlom:** Funding acquisition (equal); Supervision (equal); Writing – review & editing (equal).

DATA AVAILABILITY

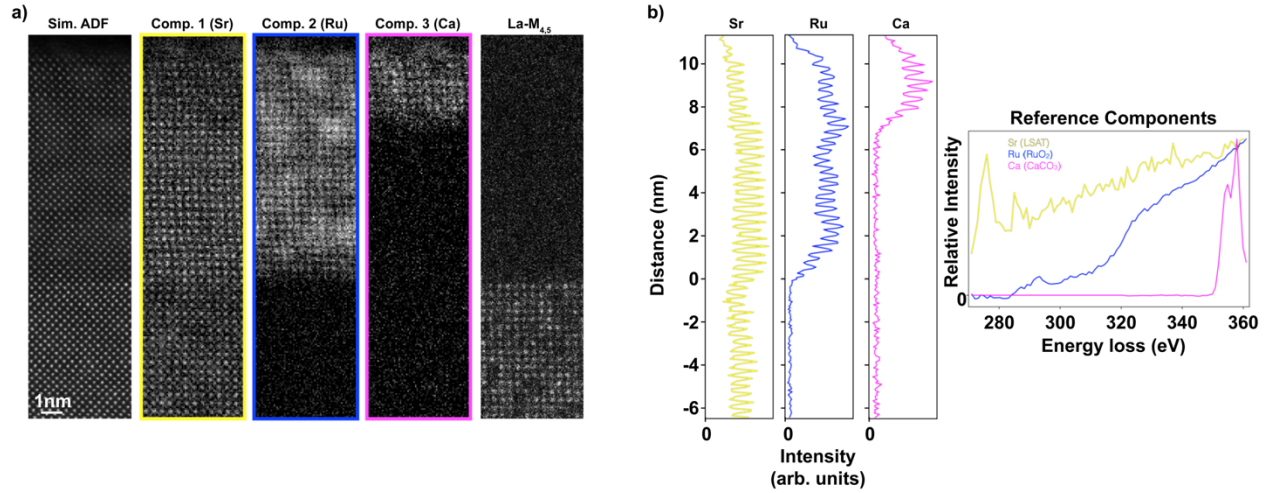
The data that support the findings of this study are available within the article. Additional data related to the film growth and structural characterization are available in the Platform for the

Accelerated Realization, Analysis, and Discovery of Interface Materials (PARADIM) database (<https://doi.org/10.34863/36tx-c606>).

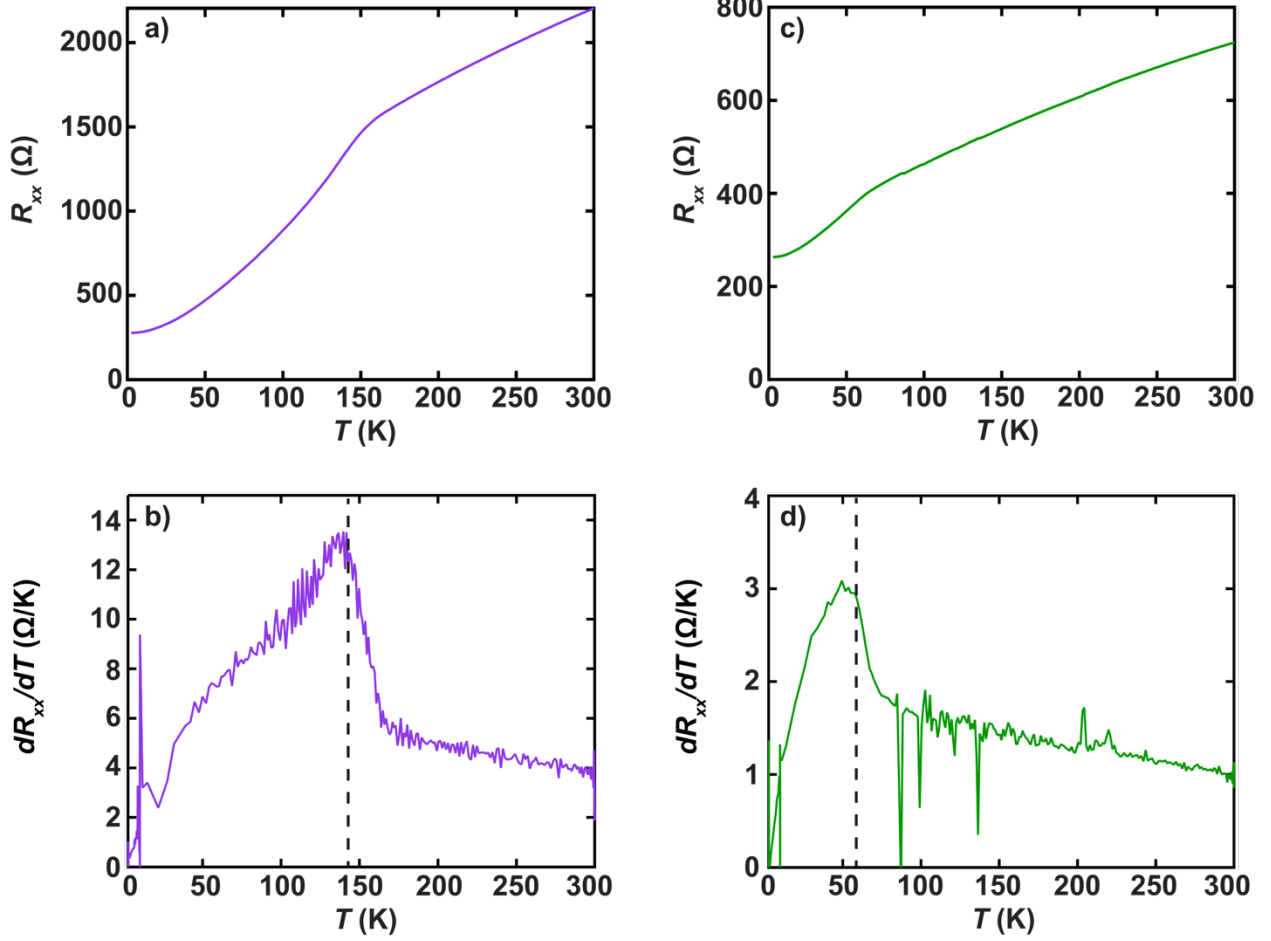
REFERENCES

- E. H. Hall, *Am. J. Math.* **2**, 287 (1879).
- N. Nagaosa, J. Sinova, S. Onoda, A. H. MacDonald, and N. P. Ong, *Rev. Mod. Phys.* **82**, 1539 (2010).
- P. Bruno, V. Dugaev, and M. Taillefumier, *Phys. Rev. Lett.* **93**, 096806 (2004).
- R. Karplus and J. M. Luttinger, *Phys. Rev.* **95**, 1154 (1954).
- X. Yu, J. P. DeGrave, Y. Hara, T. Hara, S. Jin, and Y. Tokura, *Nano Lett.* **13**, 3755 (2013).
- A. Fert, N. Reyren, and V. Cros, *Nat. Rev. Mater.* **2**, 17031 (2017).
- S. Mühlbauer, B. Binz, F. Jonietz, C. Pfleiderer, A. Rosch, A. Neubauer, R. Georgii, and P. Böni, *Science* **323**, 915 (2009).
- G. Kimbell, C. Kim, W. Wu, M. Cuoco, and J. W. A. Robinson, *Commun. Mater.* **3**, 19 (2022).
- J. Matsuno, N. Ogawa, K. Yasuda, F. Kagawa, W. Koshibae, N. Nagaosa, Y. Tokura, and M. Kawasaki, *Sci. Adv.* **2**, e1600304 (2016).
- K.-Y. Meng, A. S. Ahmed, M. Bačani, A.-O. Mandru, X. Zhao, N. Bagués, B. D. Esser, J. Flores, D. W. McComb, H. J. Hug, and F. Yang, *Nano Lett.* **19**, 3169 (2019).
- Y. Ohuchi, J. Matsuno, N. Ogawa, Y. Kozuka, M. Uchida, Y. Tokura, and M. Kawasaki, *Nat. Commun.* **9**, 213 (2018).
- L. Wang, Q. Feng, Y. Kim, R. Kim, K. H. Lee, S. D. Pollard, Y. J. Shin, H. Zhou, W. Peng, D. Lee, W. Meng, H. Yang, J. H. Han, M. Kim, Q. Lu, and T. W. Noh, *Nat. Mater.* **17**, 1087 (2018).
- W. Wang, M. W. Daniels, Z. Liao, Y. Zhao, J. Wang, G. Koster, G. Rijnders, C.-Z. Chang, D. Xiao, and W. Wu, *Nat. Mater.* **18**, 1054 (2019).
- D. Kan, T. Moriyama, K. Kobayashi, and Y. Shimakawa, *Phys. Rev. B* **98**, 180408(R) (2018).
- D. Kan and Y. Shimakawa, *Phys. Status Solidi B* **255**, 1800175 (2018).
- G. Malsch, D. Ivaneyko, P. Milde, L. Wysocki, L. Yang, P. H. M. van Loosdrecht, I. Lindfors-Vrejoiu, and L. M. Eng, *ACS Appl. Nano Mater.* **3**, 1182 (2020).
- L. Miao, N. J. Schreiber, P. HariNair, B. H. Goodge, S. Jiang, J. P. Ruf, Y. Lee, M. Fu, B. Tsang, Y. Li, C. Zeledon, J. Shan, K. F. Mak, L. F. Kourkoutis, D. G. Schlom, and K. M. Shen, *Phys. Rev. B* **102**, 064406 (2020).
- G. Kim, K. Son, Y. E. Suyolcu, L. Miao, N. J. Schreiber, H. P. Nair, D. Putzky, M. Minola, G. Christiani, P. A. van Aken, K. M. Shen, D. G. Schlom, G. Logvenov, and B. Keimer, *Phys. Rev. Mater.* **4**, 104410 (2020).
- D. J. Groenendijk, C. Autieri, T. C. van Thiel, W. Brzezicki, J. R. Hortensius, D. Afanasiev, N. Gauquelin, P. Barone, K. H. W. van den Bos, S. van Aert, J. Verbeeck, A. Filippetti, S. Picozzi, M. Cuoco, and A. D. Caviglia, *Phys. Rev. Res.* **2**, 023404 (2020).
- D. Zheng, Y.-W. Fang, S. Zhang, P. Li, Y. Wen, B. Fang, X. He, Y. Li, C. Zhang, W. Tong, W. Mi, H. Bai, H. N. Alshareef, Z. Q. Qiu, and X. Zhang, *ACS Nano* **15**, 5086 (2021).
- L. Yang, L. Wysocki, J. Schöpf, L. Jin, A. Kovács, F. Gunkel, R. Dittmann, P. H. M. van Loosdrecht, and I. Lindfors-Vrejoiu, *Phys. Rev. Mater.* **5**, 014403 (2021).
- G. Kimbell, P. M. Sass, B. Woltjes, E. K. Ko, T. W. Noh, W. Wu, and J. W. A. Robinson, *Phys. Rev. Mater.* **4**, 054414 (2020).
- L. Miao, N. J. Schreiber, Z. Liu, B. H. Goodge, L. F. Kourkoutis, H. Chen, D. G. Schlom, and K. M. Shen, "Berry curvature and magnetic anisotropy engineering in ruthenate thin films," (unpublished).
- H. P. Nair, Y. Liu, J. P. Ruf, N. J. Schreiber, S.-L. Shang, D. J. Baek, B. H. Goodge, L. F. Kourkoutis, Z.-K. Liu, K. M. Shen, and D. G. Schlom, *APL Mater.* **6**, 046101 (2018).
- D. Liang, J. P. DeGrave, M. J. Stolt, Y. Tokura, and S. Jin, *Nat. Commun.* **6**, 8217 (2015).
- Y. Ohuchi, Y. Kozuka, M. Uchida, K. Ueno, A. Tsukazaki, and M. Kawasaki, *Phys. Rev. B* **91**, 245115 (2015).

Supplementary Material



Supplementary FIG. S1. (a) Atomic-resolution mapping by electron energy loss spectroscopy of the $\text{Sr}_{0.6}\text{Ca}_{0.4}\text{RuO}_3$ [10 u.c.]/ SrRuO_3 [18 u.c.]/LSAT(100) heterostructure, showing simultaneously acquired annular dark-field (Sim. ADF) image with two-dimensional concentration maps determined by non-negative least squares (NNLS) fit to the weighted sum of reference components and by integration of the La-M_{4,5} edge. (b) Concentration profiles of the components designated to strontium, ruthenium, and calcium throughout the thickness of the heterostructure reproduced from Fig. 3. The reference components used for NNLS fits are plotted in the rightmost panel.



Supplementary FIG. S2. (a) Resistance as a function of temperature for the individual SrRuO₃[14 u.c.]/LSAT(100) film. (b) Derivative of the resistance with respect to temperature for the SrRuO₃[14 u.c.]/LSAT(100) film. The dashed line indicates the approximate T_c . (c) Resistance as a function of temperature for the individual Sr_{0.6}Ca_{0.4}RuO₃[14 u.c.]/LSAT(100) film. (d) Derivative of the resistance with respect to temperature for the Sr_{0.6}Ca_{0.4}RuO₃[14 u.c.]/LSAT(100) film. The dashed line indicates the approximate T_c .

In the model discussed in the main text, we assume a parallel resistor model with two channels from each epitaxial layer respectively. The bilayer conductances (S_{xx} and S_{xy}) are the sums of the corresponding longitudinal and transverse conductances of each layer. The transverse conductance (S_{xy}) and the transverse resistance (R_{xy}) satisfy the following relationship:

$$S_{xy} = \frac{R_{xy}}{R_{xy}^2 + R_{xx}^2} \quad (\text{S1})$$

The model is used to validate the concept of two parallel resistors of opposite AHE sign yielding a hump-like feature in the Hall measurement.